

The PSR J1124-5916 wind nebula in the near-infrared [★]

Sergey V. Zharikov¹, Dmitry A. Zyuzin², Yuri A. Shibano^{2,3}, Ronald E. Mennickent⁴

¹ Instituto de Astronomía, Universidad Nacional Autónoma de México, Ensenada, Mexico
e-mail: zhar@astrosen.unam.mx

² Ioffe Physical Technical Institute, Politekhnikeskaya 26, St. Petersburg, 194021, Russia
e-mail: dima_zyuz@mail.ru

³ St. Petersburg State Polytechnical Univ., Politekhnikeskaya 29, St. Petersburg, 195251, Russia
e-mail: shib@astro.ioffe.ru

⁴ Departamento de Astronomía, Universidad de Concepción, Casilla 160-C, Concepción, Chile
e-mail: rmennick@astro-udec.cl

Received ...; accepted ...

ABSTRACT

Context. The young radio pulsar J1124-5916 is associated with a Cas A like supernova remnant G292.0+1.8. It powers a compact torus-like pulsar wind nebula with a jet first detected in X-rays and then identified in the optical and mid-infrared.

Aims. We carried out deep near-infrared observations of the pulsar field to identify the pulsar and its nebula in this range.

Methods. The direct imaging mode of the NACO adaptive optics instrument at the ESO VLT in the H and K_s bands was used.

Results. In both bands we detected a faint, $H = 21.30(10)$ and $K_s = 20.45(10)$, extended elliptical object, whose center position is consistent with the X-ray position of the pulsar. The morphology of the object and the orientation of its major axis are in a good agreement with those observed for the pulsar torus-like nebula in the mid-infrared, optical, and X-rays. This suggests that it is the near-infrared counterpart of the nebula. The measured fluxes compiled with the data in other ranges show a complicated unabsorbed power law spectrum of the torus-like nebula with several steep breaks between the near-infrared and mid-infrared, the optical and X-rays, and possibly in the mid-infrared. This implies a multiple relativistic particle population responsible for the synchrotron emission of the nebula in different spectral ranges. We have not resolved the pulsar counterpart from its nebula and place only upper limits on its brightness, $H \geq 23.9$ and $K_s \geq 22.7$. Based on that, its contribution to the total near-infrared flux of the pulsar+nebula system is $\leq 10\%$, which is comparable with the expected contribution in the optical.

Key words. pulsars: general – pulsars, individual: PSR J1124-5916 – stars: neutron

1. Introduction

PSR J1124-5916 was discovered in the radio by Camilo et al. (2002) and in X-rays by Hughes et al. (2001, 2003) and then detected in γ -rays by Abdo et al. (2010). It is associated with the supernova remnant (SNR) G292.0+1.8 (MSH 11-54). The characteristic age of the pulsar $\tau \approx 2900$ yr and its spin-down luminosity $\dot{E} \approx 1.2 \times 10^{37}$ ergs s⁻¹ rank this pulsar as the sixth youngest and the twelfth most energetic among all rotation-powered pulsars known. The pulsar age is consistent with 2700–3700 yr age of G292.0+1.8 (Camilo et al. 2002; Chevalier 2005). The remnant low distance limit of 3.2 kpc is based on the HI absorption to beyond the tangent point in this direction (Caswell et al. 1975). An upper limit of 11 kpc follows from the pulsar dispersion measure (DM) of 330 pc cm² and Taylor & Cordes (1993) model, while 6.3 ± 0.9 kpc is considered as the most plausible distance estimate (Gaensler & Wallace 2003).

As the Crab, PSR J1124-5916 powers a compact, $\sim 5''$, and relatively bright torus-like X-ray pulsar wind nebula (PWN) with a jet (Hughes et al. 2001; Safi-Harb & Gonzalez 2002; Hughes et al. 2003; Park et al. 2007), which is surrounded by a fainter and more extended, $1' \times 2'$, plerion visible in the radio and X-rays (Gaensler & Wallace 2003). The torus-like PWN ap-

pears to be seen nearly edge-on. Its brightest inner part containing the pulsar was identified in the optical VRI bands by Zharikov et al. (2008) and then in the mid-infrared (mid-IR) at 4.5 and 8 μ m (Zyuzin et al. 2009). The point-like pulsar was not resolved from the PWN in these ranges and its contribution to the total pulsar+PWN system emission was estimated to be $\leq 20\%$. The measured fluxes implied a double-knee spectral break in the power-law spectrum of the system between the optical and X-rays. This is distinct from the Crab PWN whose spectrum shows only a single break in the same range. To obtain more stringent constraints on the optical-IR spectral energy distribution of the system, near-infrared (near-IR) observations are necessary.

Here we present the results of such observations obtained in the HK_s bands with the adaptive optic (AO) system at the ESO Very Large Telescope (VLT). We use also archival optical and mid-IR data obtained with the HST and AKARI. The observations and archival data are described in Sect. 2, the results are presented and discussed in Sect. 3 & 4 and concluded in Sect. 5.

2. VLT observations and archival data

2.1. The VLT observations, data reduction, and calibration

We observed PSR J1124-5916 in service mode in March 19, 20, 22, April 1, 11 and June 17, 18 2010 from the ESO Paranal Observatory with the NAOS CONICA (NACO), the AO near-IR imager and spectrometer mounted at the VLT Yepun unit. In order

[★] Based on observations made with ESO telescope at the Paranal Observatory under Programme 084.D-0617(A).

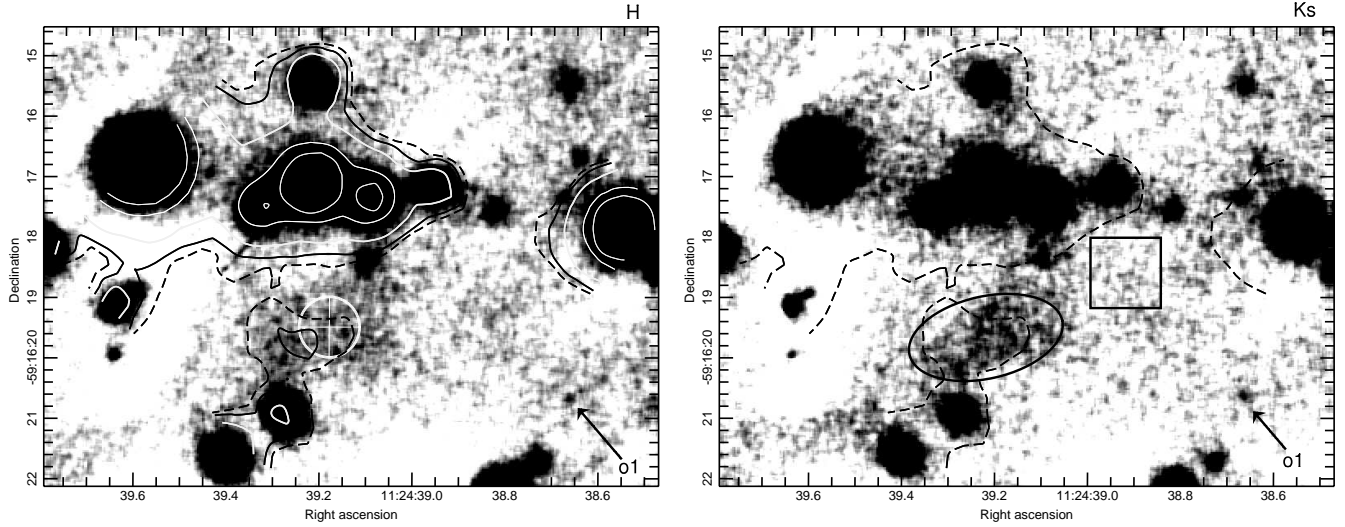


Fig. 1. VLT/NACO H (left) and K_s (right) images of the PSR J1124-5916 field smoothed with a Gaussian kernel of 3×3 pixels. The cross and circle in the H image are the X-ray pulsar position and its 1σ uncertainty. The faint object "o1" is detected in both bands and its magnitudes are accepted as stellar-like object detection limits of the images. The contours are overlaid from the V band image (Zharikov et al. 2008). The ellipse and rectangle in the K_s image show the aperture and background region, respectively, used for the PWN photometry.

Table 1. Log of the VLT/NACO observations of PSR J1124-5916.

Date (UT)	Band	AM	Seeing	NACO FWHM	Zero- point
2010-03-20	K_s	1.23	0.84(5)	0.15(3)	23.15(5)
2010-03-21	K_s	1.22	1.26(6)	0.28(3)	23.12(3)
-	K_s	1.26	1.31(13)	0.27(8)	-
2010-03-23	K_s	1.27	0.88(10)	0.38(6)	23.17(2)
2010-04-11	K_s	1.28	1.39(40)	0.28(17)	23.17(2)
2010-06-18	K_s	1.36	0.67(6)	0.34(4)	23.17(2)
2010-03-23	H	1.23	0.93(7)	0.40(3)	24.12(3)
2010-04-02	H	1.27	0.90(16)	0.24(6)	24.16(2)
2010-06-16	H	1.26	1.10(12)	0.42(5)	24.16(2)
2010-06-17	H	1.33	1.05(15)	0.49(3)	
-	H	1.50	0.89(5)	0.43(3)	
2010-06-18	H	1.27	0.57(7)	0.32(4)	

Each line in the table corresponds to an observational block of ten individual dithered exposures with integration times of 114×2 s. Block averaged airmasses (AM), seeing and AO corrected FWHMs (in arcseconds), and zero-points (in magnitude) are shown; numbers in brackets are 1σ uncertainties.

to provide the best combination between angular resolution and sensitivity, we used the S27 camera which has a pixel scale of $0''.027$ and a field of view (FOV) of $28'' \times 28''$. As a reference for the AO correction we used the GSC-2 star S11131211160 ($V, R \sim 16$ mag), located $7''.9$ away from our target. The visual dichroic element and wavefront sensor were used. The observational log is given in Table 1. The conditions were photometric with seeing varying from $0''.6$ to $1''.3$.

Day (darks, lamp flat-fields) and night time (twilight flat-fields) calibration frames were taken daily as a part of the NACO calibration plan and used to create "master" dark and flat-field frames for each of the observational blocks (OBs). Standard data reduction of science frames, including dark subtraction, flat-fielding, cosmic-ray removal, and exposure dithering correction, was performed. To remove image backgrounds, "super-flat" frames were created for each of the OBs from a median combi-

nation of respective science images where stars were replaced by surrounding background levels. The frames were normed to unit, and the science images were then super-flat corrected, aligned to a single reference frame, and summed. At the last step we used only the best quality individual images where stellar profile $FWHMs$ are $\leq 0''.4$. This condition was satisfied for 34 H and 48 K_s frames. The resulting effective mean seeing values and integration times were $0''.3$, $0''.25$ and 7752, 10944 s for the summed H and K_s images, respectively.

Photometric standards (S273-E, S363-D, S705-D) from Persson et al. (1998) were observed each night in both bands for photometric calibration. The airmass-corrected zero points provided by the NACO pipeline (Table 1) were used for photometry of several bright stars in individual science frames. Their magnitudes were then used as secondary standards for calibration of the summed images. The resulting magnitude zero-points for the summed images are $C_H = 24^m 14(5)$; $C_{K_s} = 23^m 15(5)$. The errors include uncertainties of measurements and extinction coefficients, and marginal zero-point variations from night to night.

Astrometric referencing of the summed images in both bands was performed with the IRAF *ccmap* task. There are no suitable catalogue astrometric standards in the field and several secondary astrometric standards were used instead. Their WCS coordinates were obtained from our VLT optical images of the same field referenced by Zharikov et al. (2008). Resulting rms uncertainties of the astrometric fit are $\leq 0''.1$ for RA and Dec.

The resulting H and K_s images are shown in Fig.1. Conservative 3σ detection limits for a star-like object, $H_{3\sigma} = 23^m 4$ and $K_{3\sigma} = 22^m 3$, were derived using standard 3σ background deviations within an optimal aperture of a radius of 8 pixels ($\approx 0''.22$), where the signal to noise ratio for a stellar-like object reaches a maximum. The object marked as "o1" is one of the faintest objects reliably detected in both bands with magnitudes $H^{o1} = 23^m 95(20)$ and $K_s^{o1} = 22^m 75(20)$. Below we adopt these magnitudes as real detection limits.

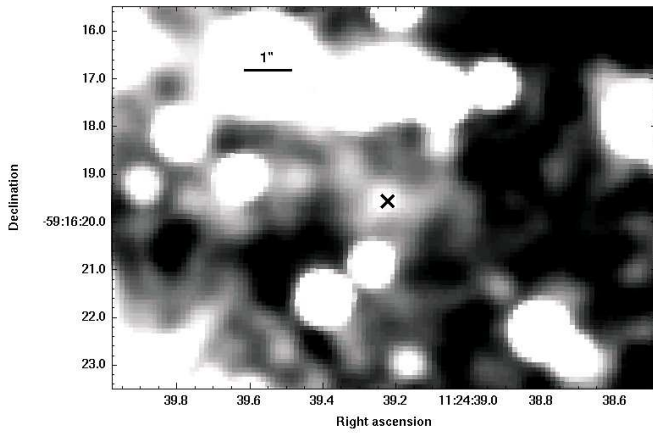


Fig. 2. Fragment of the HST/WFPC2/F675W archival image with the pulsar position indicated by "x". The image is smoothed with a 7-pix Gaussian kernel to clear the PWN, which is barely resolved, while the pulsar is not.

2.2. The HST archival data

To verify our optical fluxes of the pulsar+PWN system obtained with the VLT (Zharikov et al. 2008) we inspected the HST archive and found two detailed observations of G292.0-1.8 in various filters with the WFPC2 in 2007 and 2008. Our system is detected at $\sim 3\sigma$ level only in F675W filter images obtained in April 6 2008¹ with the total integration time of 2400 s. The data are not published. We combined the pipe-line reduced images and show the resulting image in Fig.2.

2.3. The AKARI archival data

To update the mid-IR data on the pulsar+PWN system emission reported early by Zyuzin et al. (2009) based on the Spitzer observations, we used the AKARI archival data. The AKARI mid-IR imaging of G292.0-1.8 was carried out in January 17 2007² with the Infrared Camera (IRC) equipped with an Si:As detector array with the pixel scale of $2''.51$ and $\approx 10' \times 10'$ FOV. The data with an analysis of the SNR emission have been published (Lee et al. 2009). For our analysis, we used only the images obtained with the filter centered on $15 \mu\text{m}$ (IRC L15) where the pulsar+PWN system is detected. The total on-source integration time was 180 s. The basic calibration and data handling, such as the dark-subtraction, linearity fitting, distortion correction, flat-fielding, and image combining, were performed using the IRC Imaging Data Reduction Pipeline version 070908.

3. Results

3.1. The pulsar+PWN near-IR counterpart

An extended source is clearly detected at the pulsar+PWN position in both H and K_s bands (Fig.1). It is elongated in the same SE-NW direction as the torus-like part of the PWN in other spectral domains (e.g., Zharikov et al. 2008). We are thus confident, that it is the real near-IR counterpart of the pulsar+PWN system. In the near-IR the PWN torus appears to be more extended, up to $\approx 3''.0$, than in the optical, $\approx 2''.0$, but is less extended than in the mid-IR, $\approx 10''.5$, and X-rays, $\lesssim 12''$ (cf., Zyuzin et al. 2009).

Table 2. Observed magnitudes, fluxes and de-reddened fluxes for the presumed optical/infrared PWN/pulsar counterpart of J1124-5916.

$\lambda_{eff}(\text{band})$ (μm)	Mag. observed	Log ($Flux_{obs}$) (μJy)	Log ($Flux_{A_V}$) (μJy)
0.55(V)	24.29(13)	-0.16(5)	0.66 ⁽⁺⁷⁾ ₍₋₁₃₎
0.66(R)	24.12(13)	-0.17(5)	0.51 ⁽⁺⁷⁾ ₍₋₁₂₎
0.67(F675W [†])	24.2(3)	-0.2(1)	0.57 ⁽⁺¹⁶⁾ ₍₋₁₇₎
0.77(I)	23.12(13)	0.13(5)	0.66 ⁽⁺⁷⁾ ₍₋₁₂₎
1.65(H)	21.30(10)	0.52(3)	0.66 ⁽⁺⁶⁾ ₍₋₁₀₎
2.16(K _s)	20.45(10)	0.66(3)	0.75 ⁽⁺⁶⁾ ₍₋₁₀₎
4.5	15.9(4)	1.90(21)	1.95 ⁽⁺²¹⁾ ₍₋₂₂₎
8.0	14.2(3)	2.13(16)	2.18 ⁽⁺¹⁶⁾ ₍₋₁₇₎
15	11.5(2)	2.60(8)	2.60(8)
24	≥ 10.2	≤ 2.8	≤ 2.85
70	≥ 6.8	≤ 3.2	≤ 3.2

$A_V = 1.86 - 2.10$

[†]Our estimate using the archival HST/WFPC2/F675W data

Therefore, in the near-IR, as in the optical, we see only its brightest inner part containing the pulsar.

For the counterpart photometry, we used an elliptical aperture with the center at the pulsar X-ray position and a rectangular box free of any sources to extract the source emission and backgrounds, respectively (Fig.1). The resulting magnitudes are $H^{pwn+pulsar} = 21^m30(10)$ and $K_s^{pwn+pulsar} = 20^m45(10)$. The real source boundary is apparently different from the pure elliptical one by a various way depending on the band. We account for this in the magnitude errors, which include not only statistical measurement and calibration uncertainties but also flux variations with a random shift of the ellipse center within a circular area of ~ 5 pixels radius centered at the pulsar.

To complete the PWN photometry, the HST magnitude of the pulsar+PWN optical counterpart marked by "x" in Fig.2 was estimated as $m_{F647W} = 24^m2(3)$. This marginal detection is compatible with the R-band magnitude obtained by us from deeper VLT observations (Zharikov et al. 2008). The magnitude of the system estimated from the AKARI $15 \mu\text{m}$ data is $m_{15\mu\text{m}} = 11^m5(2)$. This corresponds to the flux $\log F_\nu[\mu\text{Jy}] = 2.6 \pm 0.08$. It may be overestimated due to possible contribution of unresolved stars located near the PWN boundary, but can be taken as a confident upper limit on the system flux in this band. The measured and available observed counterpart magnitudes, fluxes in physical units, and de-reddened fluxes for a most plausible interstellar extinction range of $1^m86 \leq A_V \leq 2^m10$ (Zharikov et al. 2008) are collected in Table 2.

3.2. PWN knots and searching for the pulsar counterpart

As seen from zoomed in fragments of the near-IR images (Fig. 3), the PWN brightness spatial distribution is not uniform. Some relatively bright "knots", marked as H1—H4 and K1—K5, are visible within the 1σ error-circle of the pulsar X-ray position, where the maximum of the brightness in the optical and X-rays is located. The knots are resolved neither in the optical nor in X-rays due to significantly lower spatial resolution or a shallow exposure, as in the HST case. They cannot be due to the detector noise, since such structures are not visible in other image parts. Not all of them are surely cross-identified in both bands, while the pairs H1/K1, H2/K2, and H4/K4 likely have the same origins. The knot H1/K1 is located just at the PWN optical brightness maximum and could be a candidate to the pulsar

¹ GO 10916, PI R. Fesen

² Observation ID 1400749, PI H. Kaneda

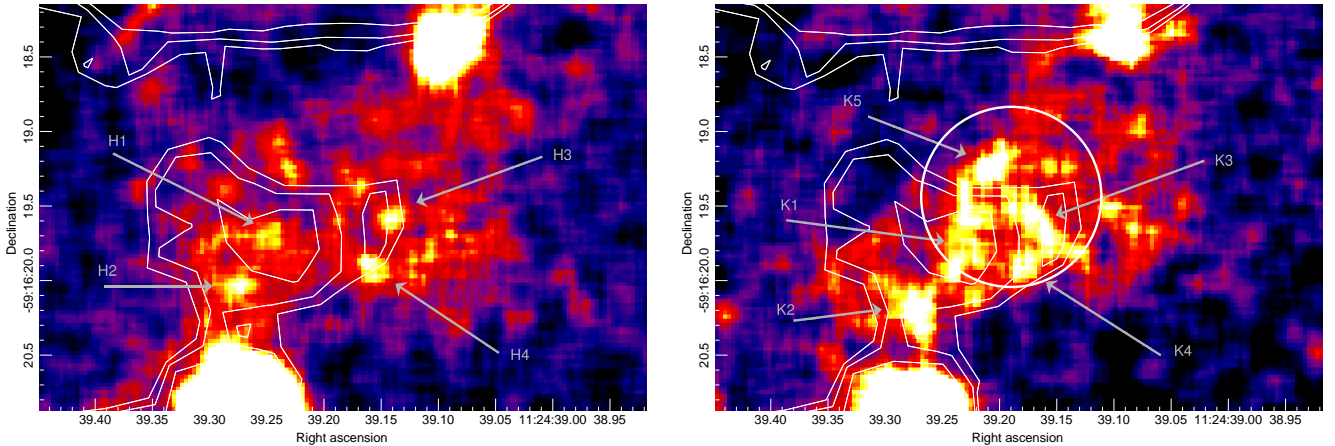


Fig. 3. H (left) and K_s (right) image fragments zoomed in on the X-ray pulsar position whose 1σ error is shown by the circle. The images are smoothed with a Gaussian 3×3 pixel kernel, and their horizontal sizes are $\sim 4''.5$. As in Fig. 1, the contours are from the V band image, they show the structure of the PWN in the optical. Several relatively bright knots nearly the pulsar position are marked by H1-H4 and K1-K5.

counterpart. Others are likely to be compact synchrotron structures formed in the PWN torus as is in the Crab case. Alternatively, the knots might be a SN ejecta that has been shocked by the PWN. For instance, Zajczyk et al. (2012) reported on FeII emission from G21.9-0.9 in the $1.64 \mu\text{m}$ narrow band overlapping with the H band. It forms a shell-like structure around the G21.9-0.9 PWN X-ray boundary. Similar narrow band studies of the G292.0+1.8 field are necessary to establish whether the knots visible inside its PWN torus are related to the shocked ejecta or not. The knots could also be faint unrelated background sources projected on the PWN. However, this is very unlikely due to a much smaller surface density of such sources in other parts of the field.

The local background in the PWN area is higher than that around faintest isolated objects outside it, for instance, around source o1 in Fig. 1. This precludes us to confidently measure the knot magnitudes relative to the local background with an accuracy of better than $0^{\text{m}}.3$. A conservative estimate yields that their fluxes are about or a few less of the source o1 flux, which is firmly detected at a 5σ significance in both bands (Sect. 2.1). Based on that, the knot and pulsar brightness upper limits are $H^{psr} \gtrsim 23^{\text{m}}.9$ and $K_s^{psr} \gtrsim 22^{\text{m}}.7$. The contribution of the cross-identified knots H1/K1, H2/K2, and H4/K4 to the derived total pulsar+PWN-torus fluxes is estimated to be $\lesssim 30\%$. Since the SN ejecta origin of the knots is questionable and they do not dominate the entire pulsar+PWN flux, below we focus only on the analysis of the spatially integrated fluxes derived above.

4. Discussion

VLT NACO observations allowed us to detect the near-IR counterpart of the compact torus-like structure of the J1124-5916 PWN in the H and K_s bands and measure its spatially integrated fluxes. This makes J1124-5916 the fifth, after the Crab (Grasdalen 1979), G21.5-09 (Zajczyk et al. 2012), B540-69 (Mignani et al. 2012), and 3C 58 (Zyuzin et al., in preparation), among other PWNe ever identified in the near-IR.

A high spatial resolution of $\lesssim 0''.3$ provided by the NACO, allowed us to resolve a fine structure of the PWN whose spatial brightness distribution is nonuniform. It contains several relatively bright knots located within or near the pulsar 1σ X-ray position error circle. Three of them are cross-identified in the H

and K_s bands, and one of three, H1/K1, is possibly associated with the pulsar. A high PWN background precludes a confident knot flux extraction, and we derive only flux upper limits, showing that the pulsar contribution to the total pulsar+PWN flux in the near-IR is $\lesssim 10\%$. In addition, the AKARI and HST archival data allowed us to constrain the PWN mid-IR flux at $15 \mu\text{m}$ and confirm its optical flux. Below we discuss possible implications of the results.

4.1. Multiwavelength spectrum of the torus-like PWN

In Fig. 4 the spectrum of the J1124-5916 torus PWN compiled from the data obtained here and published early by Zyuzin et al. (2009) is compared with available spectra³ for other four torus-like PWNe mentioned above. All of them, except for a highly absorbed G21.5-09, are also identified in the optical. The spectra are non-thermal, as expected for the synchrotron origin of the PWN emission, and can be described by power laws with different spectral indexes α_ν (defined as $F_\nu \propto \nu^{\alpha_\nu}$) depending on the spectral domain. All of them show a strong flux increase towards low frequency range. For the youngest Crab, and possible for G21.5-09⁴, the increase appears to be monotonic with a gradual spectral slope decrease towards the IR⁵. While for the older J1124-5916 we see at least two strong spectral breaks: one is between the optical and X-rays and another is between the near-IR and mid-IR. The third possible break exists above $15 \mu\text{m}$ with slope flattening towards lower frequencies. A sharp, likely a double knee break between the optical and X-rays is visible in the spectrum of a similar age 3C 58 PWN (Shibanov et al.

³ The data are taken: for the Crab from Green et al. (2004), Temim et al. (2006), Grasdalen (1979), Veron-Cetty & Woltjer (1993), and Kirsch et al. (2005); for G21.5-0.9 from Zajczyk et al. (2012); for B0540-69.3 from Manchester et al. (1993), Williams et al. (2008), Mignani et al. (2012), and Serafimovich et al. (2005); for 3C 58 from Shibanov et al. (2008), Shearer & Neustroev (2008), and Slane et al. (2008).

⁴ We indicate in the plot the SNR (870 yr, Bietenholz & Bartel 2008) and spindown (4800 yr, Camilo et al. 2006) ages for this PWN.

⁵ A mid-IR bump over the power law fit in the Crab spectrum in the mid-IR at $\sim 50 \mu\text{m}$ is due to thermal emission from a warm dust created by the SN (Temim et al. 2006; Arendt et al. 2011; Temim et al. 2012).

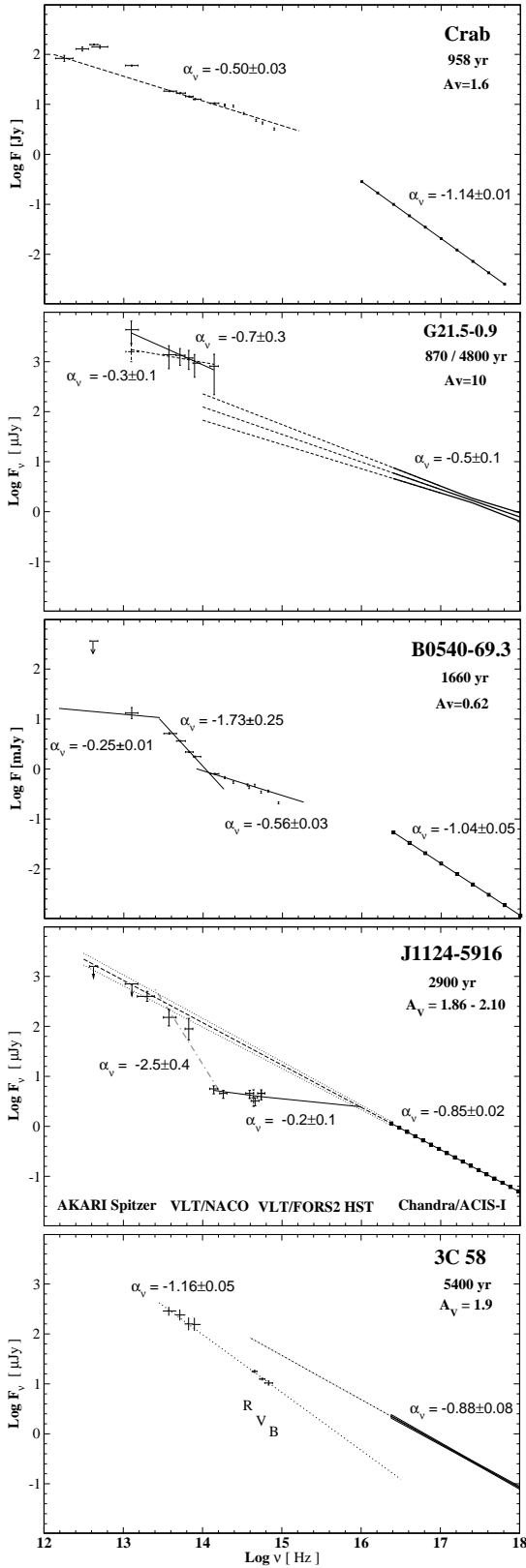


Fig. 4. Multi-wavelength spectra of torus-like PWNe obtained with different instruments and ordered by PWN age from top to bottom.

2008)⁶. The spectrum of B0540-69, which is slightly older than the Crab, becomes apparently steeper in the mid-IR, as com-

⁶ The optical-IR part of the 3C 58 torus spectrum is confirmed by near-UV and near-IR observations (Zyuzin et al., in preparation).

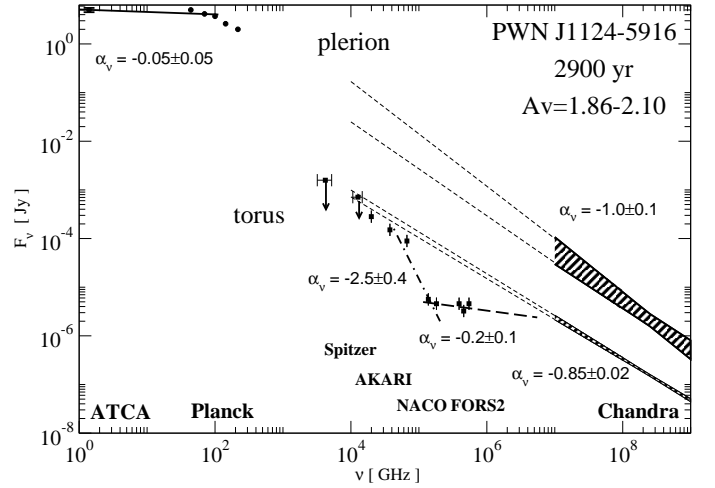


Fig. 5. Comparison of the spatially integrated multiwavelength spectra of the J1124-5916 PWN for the compact PWN torus (lower curves) and for the much more extended plerion (upper curves) obtained with different instruments, as notified in the plot. The radio and submillimetre data for the plerion are taken from Gaensler & Wallace (2003) and Planck Collaboration et al. (2011), respectively. 1σ X-ray uncertainties for each of the spectrum are indicated by hatched regions and they are extended towards low frequency range. The torus is not detected in the radio, while the plerion is not identified in the IR.

pared to the optical-near-IR, suggesting a break at a few microns (Mignani et al. 2012), and then flattens again at longer wavelengths (Williams et al. 2008). A double knee break between the optical and X-rays is also not excluded (Serafimovich et al. 2005). At the same time, the IR part of the G21.5-09 spectrum is likely to be almost flat⁷, implying at least one break between the IR and X-rays (Zajczyk et al. 2012).

We can conclude that the presence of several prominent spectral breaks in the IR-optical-X-ray range is a common feature for torus-like PWNe. This cannot be excluded even for the Crab, where, in addition to the significant X-ray-optical slope change, some small breaks may exist between the optical and near-IR and/or between the near-IR and mid-IR (Arendt et al. 2011). In Fig. 4 the breaks likely become stronger with PWN age. However, this apparent spectral evolution trend has to be considered with a caution, since the spectrum of the Crab is dominated by the small torus region only in X-rays, while at low frequencies it includes the emission from the whole plerion resulting to the smoothness of the spectrum. The same problem is not solved yet for the Crab "twin", B0540-69, whose PWN torus is not yet firmly resolved and its position and orientation are still debated (De Luca et al. 2007; Lundqvist et al. 2011).

It is evident that the compact torus-like PWN works as an energy injector for the large scale plerion. As mentioned by Gaensler & Wallace (2003), the spectrum of the J1124-5916 large scale plerion has a single spectral break between the radio and X-rays with $\Delta\alpha_v \sim 1$ at a relatively low frequency range of $\lesssim 800$ GHz. The Planck early release compact source catalog⁸ allows us to constrain more precisely the break position

⁷ We remeasured the Spitzer fluxes for this PWN and found a good agreement with Zajczyk et al. (2012) for all bands except for $24 \mu\text{m}$, where our flux of (1.58 ± 0.81) mJy, is by a factor of 3 lower than their one and consistent with more flat spectral index derived using lower wavelength bands. The reasons for the discrepancy are unclear, and in Fig. 4 we show both measurements for this band and respective fits.

⁸ astro-ph arXiv:1101.2041

Table 3. H and K_s magnitudes, near-IR luminosities L_{IR} , and radiation efficiencies η_{IR} of radio pulsars observed in the near-IR.

Pulsar name	$\log \tau$	$\log \dot{E}$	distance	A_V	H, K_s mag	$\log L_{IR}$	$\log \eta_{IR}$	Ref.
Crab	3.1	38.65	1.73(28)	1.62	14.27(5), 13.77(5)	32.6(1), 32.9(1)	-6.1(1), -5.8(1)	(1)
PSR 0540-69	3.2	38.17	5×10^4	0.62	19.33(10), 18.55(10)	33.2(1), 33.3(1)	-5.0(1), -4.9(1)	(2)
PSR B1509-58	3.2	37.25	5.2(1.4)	4.8	20.6(2), 19.4(1)	31.1(2), 31.6(1)	-6.2(2), -5.7(1)	(3)
PSR J1124-5916	3.5	37.08	~ 6.0	1.98(12)	$\geq 23.9, \geq 22.7$	$\leq 29.8, \leq 29.9$	$\leq -7.3, \leq -7.2$	tw
Vela	4.1	36.84	$0.293^{+0.019}_{-0.017}$	0.20	22.04(16), 21.3(4)	27.7(1), 28.1(2)	-9.1(1), -8.7(2)	(4)
PSR B0656+14*	5.0	34.58	$0.288^{+0.033}_{-0.027}$	0.09(6)	23.22(8), 22.63(13)	27.3(1), 27.6(1)	-7.3(1), -7.0(1)	(5)
Geminga*	5.5	34.51	$0.157^{+0.059}_{-0.034}$	0.12(9)	24.30(10), 23.4(4)	26.3(1), 26.7(2)	-8.2(1), -7.7(2)	(5)

(*) based on the HST F110W and F160W band observations;

(1) Sollerman (2003); (2) Mignani et al. (2012); (3) Kaplan & Moon (2006); (4) Shibano et al. (2003); (5) Koptsevich et al. (2001)

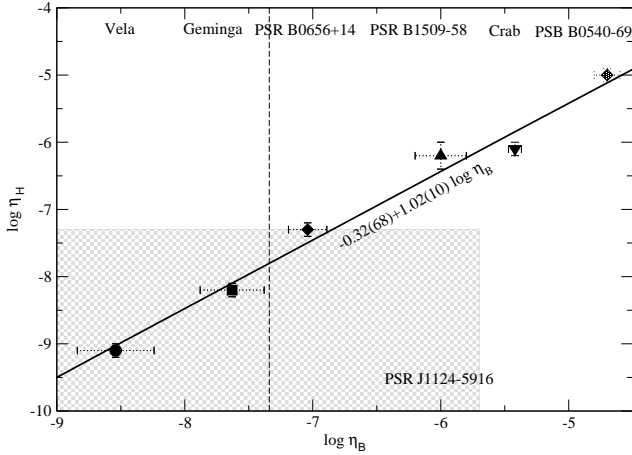


Fig. 6. Correlation between the optical (B band) and near-IR (H band) efficiencies of radio pulsars. The optical data are taken from Zharikov et al. (2006).

near 70 GHz, where the plerion flux of (4.1 ± 0.2) mJy becomes significantly lower than that of (5.3 ± 0.1) mJy at 5 GHz measured early, and continues to drop rapidly with the frequency (e.g., (2.1 ± 0.1) mJy at 217 GHz; Fig. 5). In Fig. 5 the X-ray spectrum of the G292.0+1.8 plerion was obtained using the data from the Chandra archive⁹. We reprocessed "level 1" data with CIAO chandra_repro script and used the spectral interval of 5 – 10 keV to exclude the G292.0+1.8 thermal component strongly dominating the nonthermal plerion spectrum at smaller energies. The spectrum was extracted using a source aperture of 1' centered at the pulsar, background was taken outside the SNR, and fitted by a single absorbed power law with a resulting slope $\alpha_\nu = -1.0(1)$. The low frequency spectral break of the plerion cannot be simply explained by synchrotron losses of a single particle population (Gaensler & Wallace 2003), suggesting, as is in the Crab (Kennel & Coroniti 1984) and 3C 58 (Slane et al. 2008) cases, distinct populations for the radio and X-ray emission of the plerion. The observed multiple spectral breaks in the torus emission serve as the direct evidence of a complicated spectrum of the injected particles, which cannot be described by a simple model of an unbroken powerlaw. This fact can help us to better understand the nature of the low-frequency break of the large scale plerion for J1124-5916 and similar breaks for other PWNe. To do that more detail observations of PWNe and modeling of these systems are necessary.

⁹ ID 6677, PI S. Park

4.2. Pulsar flux upper limits and efficiencies

In Table. 3 we summarize observed H, K_s magnitudes, respective luminosities and radiation efficiencies $\eta = L_{IR}/\dot{E}$ of rotation powered pulsars detected in the near-IR and optical bands. The H vs. B band efficiency plot (Fig. 6) shows a strong correlation between the optical and near-IR efficiencies. This confirms a common origin of radiation in the near-IR and the optical resulting also from rather smooth pulsar spectral energy distributions in these ranges. The $\eta_H \propto \eta_B$ empirical relationship derived from the plot (thick solid line) allows one to predict IR magnitudes for all pulsars which have been detected in the optical but not yet in the near-IR and vice versa.

Based on the observed PSR J1124-5916 flux upper limits in the near-IR obtained here and in the optical provided by Zharikov et al. (2008), we can constrain the pulsar position region on the efficiency plain (shaded region in Fig. 6) and conclude that its efficiencies are at least lower than those of younger pulsars. The $\eta_H \propto \eta_B$ relationship and the H band limit suggest that the pulsar cannot be more efficient than the middle-aged PSR B0656+14, and allows us to better constrain its η_B (vertical dashed line) than it was possible from our optical observations. We predict that its de-reddened $B \geq 26^m.8$. This means also that the pulsar contribution to the total pulsar+PWN optical flux is $\leq 10\%$, as is in the near-IR.

5. Conclusions

Using the NACO at the VLT we performed the deepest up to date near-IR observations of the young pulsar J1124-5916 field. In the H and K_s bands we detected a faint $H = 21.30(10)$, $K_s = 20.45(10)$ extended elliptical object, whose center position is consistent with the X-ray position of the pulsar. The morphology of the object and the orientation of its major axis are in a good agreement with those for the J1124-5916 torus-like PWN obtained in the optical and X-rays. This allows us to conclude that we detected the near-IR counterpart of the PWN. The compiled IR-optical-X-ray power-law spectrum of the torus-like PWN shows several spectral breaks implying a multiple population of relativistic particles responsible for the emission in different spectral domains. This may help to explain a single low frequency break in the radio-X-ray spectrum of the large scale plerion of J1124-5916, which is impossible to describe by a single particle population. The presence of several spectral breaks appears to be a common feature for the spectra of all torus-like PWNe.

We found several faint knot-like objects nearly the X-ray position of the pulsar. The PWN background is high in this area, which has not allowed us to conclude confidently about their origin. We derived the upper limits for the pulsar near-IR fluxes and

estimated its contribution to the total pulsar+PWN flux in this range at a level of $\leq 10\%$. Comparing to other pulsars observed in the near-IR and optical we conclude, that the expected pulsar contribution in the optical should not also exceed this level. Deeper high-spatial resolution optical and near-IR observations are necessary to resolve the pulsar from its PWN.

Acknowledgements. The work was partially supported by CONACYT 151858 projects and by the Russian Foundation for Basic Research (grants 11-02-00253 and 13-02-12017-ofi-m), RF Presidential Program (Grant NSh 4035.2012.2). REM acknowledges support by the BASAL Centro de Astrofísica y Tecnologías Afines (CATA) PFB-06/2007.

References

- Abdo, A. A., Ackermann, M., Ajello, M., et al. 2010, *ApJS*, 187, 460
 Arendt, R. G., George, J. V., Staguhn, J. G., et al. 2011, *ApJ*, 734, 54
 Bietenholz, M. F. & Bartel, N. 2008, *MNRAS*, 386, 1411
 Camilo, F., Manchester, R. N., Gaensler, B. M., Lorimer, D. R., & Sarkissian, J. 2002, *ApJ*, 567, L71
 Camilo, F., Ransom, S. M., Gaensler, B. M., et al. 2006, *ApJ*, 637, 456
 Caswell, J. L., Murray, J. D., Roger, R. S., Cole, D. J., & Cooke, D. J. 1975, *A&A*, 45, 239
 Chevalier, R. A. 2005, *ApJ*, 619, 839
 De Luca, A., Mignani, R. P., Caraveo, P. A., & Bignami, G. F. 2007, *ApJ*, 667, L77
 Gaensler, B. M. & Wallace, B. J. 2003, *ApJ*, 594, 326
 Grasdalen, G. L. 1979, *PASP*, 91, 436
 Green, D. A., Tuffs, R. J., & Popescu, C. C. 2004, *MNRAS*, 355, 1315
 Hughes, J. P., Slane, P. O., Burrows, D. N., et al. 2001, *ApJ*, 559, L153
 Hughes, J. P., Slane, P. O., Park, S., Roming, P. W. A., & Burrows, D. N. 2003, *ApJ*, 591, L139
 Kaplan, D. L. & Moon, D.-S. 2006, *ApJ*, 644, 1056
 Kennel, C. F. & Coroniti, F. V. 1984, *ApJ*, 283, 710
 Kirsch, M. G., Briel, U. G., Burrows, D., et al. 2005, in *Society of Photo-Optical Instrumentation Engineers (SPIE) Conference Series*, Vol. 5898, Society of Photo-Optical Instrumentation Engineers (SPIE) Conference Series, ed. O. H. W. Siegmund, 22–33
 Koptsevich, A. B., Pavlov, G. G., Zharikov, S. V., et al. 2001, *A&A*, 370, 1004
 Lee, H.-G., Koo, B.-C., Moon, D.-S., et al. 2009, *ApJ*, 706, 441
 Lundqvist, N., Lundqvist, P., Björnsson, C.-I., et al. 2011, *MNRAS*, 413, 611
 Manchester, R. N., Staveley-Smith, L., & Kesteven, M. J. 1993, *ApJ*, 411, 756
 Mignani, R. P., De Luca, A., Hummel, W., et al. 2012, *A&A*, 544, A100
 Park, S., Hughes, J. P., Slane, P. O., et al. 2007, *ApJ*, 670, L121
 Persson, S. E., Murphy, D. C., Krzeminski, W., Roth, M., & Rieke, M. J. 1998, *AJ*, 116, 2475
 Planck Collaboration, Ade, P. A. R., Aghanim, N., et al. 2011, *A&A*, 536, A7
 Safi-Harb, S. & Gonzalez, M. E. 2002, in *Astronomical Society of the Pacific Conference Series*, Vol. 262, *The High Energy Universe at Sharp Focus: Chandra Science*, ed. E. M. Schlegel & S. D. Vrtilek, 315
 Serafimovich, N. I., Lundqvist, P., Shibano, Y. A., & Sollerman, J. 2005, *Advances in Space Research*, 35, 1106
 Shearer, A. & Neustroev, V. V. 2008, *MNRAS*, 390, 235
 Shibano, Y. A., Koptsevich, A. B., Sollerman, J., & Lundqvist, P. 2003, *A&A*, 406, 645
 Shibano, Y. A., Lundqvist, N., Lundqvist, P., Sollerman, J., & Zyuzin, D. 2008, *A&A*, 486, 273
 Slane, P., Helfand, D. J., Reynolds, S. P., et al. 2008, *ApJ*, 676, L33
 Sollerman, J. 2003, *A&A*, 406, 639
 Taylor, J. H. & Cordes, J. M. 1993, *ApJ*, 411, 674
 Temim, T., Gehrz, R. D., Woodward, C. E., et al. 2006, *AJ*, 132, 1610
 Temim, T., Sonneborn, G., Dwek, E., et al. 2012, *ApJ*, 753, 72
 Veron-Cetty, M. P. & Woltjer, L. 1993, *A&A*, 270, 370
 Williams, B. J., Borkowski, K. J., Reynolds, S. P., et al. 2008, *ApJ*, 687, 1054
 Zajczyk, A., Gallant, Y. A., Slane, P., et al. 2012, *A&A*, 542, A12
 Zharikov, S., Shibano, Y., & Komarova, V. 2006, *Advances in Space Research*, 37, 1979
 Zharikov, S. V., Shibano, Y. A., Zyuzin, D. A., Mennickent, R. E., & Komarova, V. N. 2008, *A&A*, 492, 805
 Zyuzin, D. A., Danilenko, A. A., Zharikov, S. V., & Shibano, Y. A. 2009, *A&A*, 508, 855